This article has been accepted for publication in IEEE Sensors Journal. This is the author's version which has not been fully edited and content may change prior to final publication. Citation information: DOI 10.1109/JSEN.2026.3692954

Accurate 3D Motion Tracking Based on Radar Distributed Network

Fabrizio L. Carcione, *Graduate Student Member, IEEE,* Paolo Brasiliano, *Member, IEEE*, Elena Bergamini, *Member, IEEE*, Emanuele Cardillo, *Senior Member, IEEE*

***Abstract*—This article examines the feasibility of measuring the three-dimensional (3D) displacement of moving targets using a distributed network of three 24 GHz Doppler radars positioned along orthogonal axes. Though radar sensors offer advantages over optical sensors in terms of cost and privacy, conventional phase-based estimation fails during stationary periods or with multi-component targets. To address these issues, this work proposes a displacement detection method based on an ad-hoc experimental setup and the micro-Doppler signature. A curve extraction algorithm isolates the different body parts, which are then integrated over time to determine displacement. The proposed method is validated through both simulation and measurements and supported by a stereophotogrammetric system as ground truth. The system's effectiveness was further demonstrated through a proof-of-concept human walking trial, proving that micro-Doppler analysis can overcome the limitations of classical phase-based methods in biomechanical applications.**

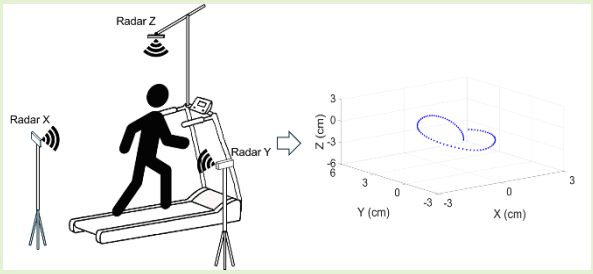

***Index Terms*—biomedical applications, center of mass, distributed network, Doppler radar, micro-Doppler signature, three-dimensional displacement.**

I. Introduction

In the past years, radar sensors have outperformed conventional mechanical and optical sensors, due to their contactless measurements and reliability under adverse lighting conditions [1], [2]. Consequently, radars have become vital in the automotive sector, industrial processing, and biomedical environments [3], [4], [5], [6], [7], [8], [9]. For displacement measurement, Doppler radars are generally preferred over frequency-modulated continuous wave (FMCW) radars, due to their simpler architecture, lower cost, reduced power consumption, lower computational complexity for data processing, and a higher detectable maximum speed [10].

The accurate displacement extraction is a critical step, and many contributions have been proposed [11], [12], [13], [14]. Frequently, displacement is extracted directly from the received signal phase [15], [16], [17]. However, this method requires additional effort when the target is stationary during the measurement, as thermal noise can dominate the signal, leading to incorrect displacement evaluation due to random phase evolution [18], [19]. Furthermore, in non-rigid body scenarios, such as human motion, the total phase is the sum of the individual phase histories, which complicates the estimation [20], [21]. Additionally, phase-based methods are highly sensitive to unexpected interference [22]. These limitations have encouraged the investigation of alternative signal representations and processing strategies [23], [24].

In a clinic environment, accurate human body displacement detection plays a fundamental role in gait analysis, motion recognition, athlete performance evaluation, rehabilitation, and diagnostics [25], [26], [27]. In this scenario, the radar sensing system is proposed as a valuable alternative technology to optical-based systems and inertial measurement units (IMUs). Optical cameras are usually limited by visual-range occlusions, require controlled lighting, and necessitate wearable markers that may alter natural gait, causing user discomfort and privacy concerns. Moreover, cameras require substantial physical space due to their arrangement in the environment [28]. On the other hand, although cheaper, IMU sensors are often affected by cumulative integration drift, due to sensor inconsistency and external factors, which compromise their accuracy [29], [30]. Instead, the radar sensor network offers a non-invasive, low-cost, space-efficient, and privacy-preserving approach.

In this context, due to the phase challenges and human

This work was funded by the European Union – NextGenerationEU, under the National Recovery and Resilience Plan (PNRR), Mission 4, Component 2, Investment 1.1, funding call PRIN 2022 D.D. 104 published on 2.2.2022 by the Italian Ministry of University and Research (Ministero dell'Università e della Ricerca), Project Title: entitled "CARAMELLA - Contactless And ReliAble MovEment anaLysis with miLlimeter-waves rAdars" – CUP J53D23000890006, ID: 2022TLSWHM.

Fabrizio Lorenzo Carcione and Emanuele Cardillo are with the Department of Engineering, University of Messina, 98100 Messina, Italy (e-mail: fcarcione@unime.it; ecardillo@unime.it).

Paolo Brasiliano is with the Department of Motor, Human and Health Sciences, University of Rome "Foro Italico", 00135 Roma, Italy (e-mail: paolo.brasiliano@uniroma4.it) and the Department of Management, Information and Production Engineering, University of Bergamo, 24129 Bergamo, Italy (e-mail: paolo.brasiliano@unibg.it).

Elena Bergamini is with the Department of Management, Information and Production Engineering, University of Bergamo, 24129 Bergamo, Italy (e-mail: elena.bergamini@unibg.it).

XXXX-XXXX © XXXX IEEE. Personal use is permitted, but republication/redistribution requires IEEE permission.
See http://www.ieee.org/publications_standards/publications/rights/index.html for more information.
This work is licensed under a Creative Commons Attribution 4.0 License. For more information, see https://creativecommons.org/licenses/by/4.0/

This article has been accepted for publication in IEEE Sensors Journal. This is the author's version which has not been fully edited and
content may change prior to final publication. Citation information: DOI 10.1109/JSEN.2026.3692954

motion complexity, time-frequency analysis is often employed [31], [32], [33]. The micro-Doppler signature provides a time-varying velocity representation, identifying different motion components for more robust tracking, even during pauses or superimposed movements [34], [35], [36], [37], [38], [39]. However, existing studies are limited to one-dimensional displacement estimation using a single radar. This configuration restricts the analysis and limits the understanding of the target dynamics in complex trajectories or multi-axis movements. In [40] and [41], a new methodology is presented to extract the target motion pattern from the micro-Doppler signature. However, both contributions present only simulated results, lacking the experimental evidence required for qualitative and quantitative comparison with our methodology.

This work explores the feasibility of reconstructing the three-dimensional displacement of a moving target by integrating measurements from three 24 GHz Doppler radar sensors positioned along orthogonal X, Y, and Z axes. Since single-input single-output radars measure only radial movements, a distributed network of three radar sensors is used to reconstruct three-dimensional (3D) motion along the three orthogonal axes. A new displacement detection technique is proposed to advance the current state of the art. The algorithm initially extracts the velocity curves from each radar micro-Doppler signature, which are subsequently integrated to obtain the three independent displacements. The validity of the new algorithm has been tested on both simulated and experimental data, including trials on a spherical moving object and evaluation involving a human subject. In the experimental setup, radar measurements were compared with those from a synchronized stereophotogrammetric system, providing an independent ground truth for precise assessment, measuring its accuracy, and highlighting the strengths and limitations of the proposed method [42].

The rest of this article is organized as follows: Section II introduces the theoretical background of Doppler radar and discusses the phase history displacement estimation method and micro-Doppler analysis. Section III details the micro-Doppler-based extraction method. Section IV covers the simulated scenario and experimental setup, analyzing the results. Finally, Section V presents the conclusion.

II. Doppler and Micro-Doppler Theory

Due to the Doppler effect, the frequency of the received signal differs from the transmitted one, providing information on the speed and displacement of the target [34]. Considering a typical block diagram of Doppler radar, as shown in Fig. 1, the transmitted constant frequency signal $S_t(t)$ is written as:

$$S_t(t)=A_t cos\ (2\pi f_c t+\phi_0) \tag{1}$$

where f_c is the carrier operating frequency, ϕ_0 is the initial phase, and A_t is the amplitude of the signal [15],[34],[36].

For a multi-component target moving along the field of view of the radar sensor, the echo signal $S_r(t)$ intercepted by the receiver is the sum of N components, and at the output of the two mixers, the in-phase $S_I(t)$ and quadrature $S_Q(t)$ signals are:

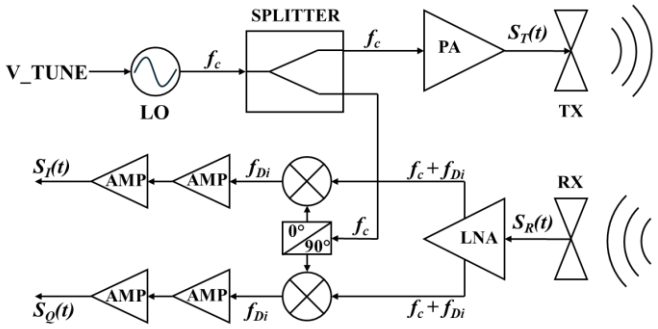

Fig. 1. Doppler radar system block diagram.

$$S_I(t)=\sum_{i=1}^{N} A_i cos\ (2\pi f_{Di} t+\phi_i) \tag{2}$$

$$S_Q(t)=\sum_{i=1}^{N} A_i sin\ (2\pi f_{Di} t+\phi_i). \tag{3}$$

where A_i and ϕ_i represent the amplitude and the phase of the i-th component of the received signal, while f_{Di} corresponds to the Doppler frequency of the i-th target component, and it is given by the expression:

$$f_{Di}=\pm\frac{2v_i cos(\psi) f_c}{c}=\pm\frac{2v_i cos(\psi)}{\lambda} \tag{4}$$

where c is the speed of light in a vacuum, λ is the wavelength, and v is the target speed. The sign indicates whether the target is approaching or moving away from the radar, whereas ψ is the angle between the velocity vector of the target component and the radar line-of-sight (LOS) [34],[36],[39].

The traditional phase-based procedure determines the phase value, $\varphi(t)$, using nonlinear arctangent quadrature demodulation, which is expressed as:

$$\varphi(t)=tan^{-1}\left(\frac{S_Q(t)}{S_I(t)}\right)=\sum_{i=1}^{N}\pm\frac{4\pi x_i(t)}{\lambda}+\frac{4\pi d_0}{\lambda}+\phi_0+n_{Ph}(t) \tag{5}$$

where $x_i(t)$ is the displacement of the i-th target component, d_0 is the initial target distance, and n_{Ph} is the phase noise [34]. It is worth noting that the term d_0 is constant, as well as ϕ_0. Therefore, the displacement is accurately estimated when the target is in motion, and the signal-to-noise ratio is sufficiently high. Nevertheless, during the stationary period of the target, $x_i(t) = 0$, the phase noise dominates the received signal's phase $\varphi(t)$, leading to incorrect displacement evaluation. Furthermore, the phase-based displacement measurement inherently includes every motion of a multi-component target, making it challenging to distinguish individual components [15], [18].

To overcome these limitations, the micro-Doppler analysis method can be used. Multiple target movements create a Doppler modulation, leading to extra spectral components around the main Doppler frequency. To retain the time-frequency features of the signal, the Short-Time Fourier

This work is licensed under a Creative Commons Attribution 4.0 License. For more information, see https://creativecommons.org/licenses/by/4.0/

This article has been accepted for publication in IEEE Sensors Journal. This is the author's version which has not been fully edited and content may change prior to final publication. Citation information: DOI 10.1109/JSEN.2026.3692954

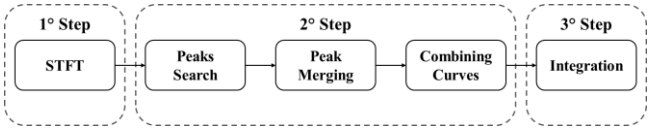

Fig. 2. Block diagram for the displacement extraction method.

Transform (STFT) is applied, producing a spectrogram that shows how the frequency components change over time. The STFT of the beat signal $S_b(t) = S_I(t) + jS_Q(t)$ is expressed as:

$$STFT(t,f) = \int_{-\infty}^{+\infty} S_b(\tau)\, w(\tau - t) e^{-j2\pi f\tau} d\tau \quad (6)$$

where w is the short-time window function [33],[35].

It is worth noting that the choice of window function and its size determine the trade-off between time and frequency resolution of the spectrogram.

III. Displacement Extraction Method

As shown in Fig. 2, to extract the displacement information from the micro-Doppler signature, three fundamental steps are required:

1) Obtain the micro-Doppler matrix from the raw signal.
2) Apply the extraction algorithm on the micro-Doppler matrix.
3) Integrate the extracted velocity curves to obtain the displacement.

A. Micro-Doppler Matrix Evaluation

To achieve a suitable trade-off between time and frequency resolutions, the STFT employs a Hamming window with a duration of 0.1 s and an overlap of 90%. Moreover, for long-duration records, applying the STFT to the entire signal can be computationally impractical. Therefore, the Micro-Doppler analysis is performed on consecutive 3 s signal segments. This segmentation introduces inaccuracies at the boundaries of each 3 s block. To address this discontinuity, an overlap of 0.2 s is adopted between consecutive segments. This results in a shift of 2.8 s between the start of each STFT calculation. For example, in a 12s signal, the STFT is computed over the intervals [0 – 3] s, followed by [2.8 – 5.8] s, [5.6 – 8.6] s, and [8.4 – 11.4] s. The final time interval, starting at 11.2 s, is not processed as its remaining duration is insufficient for the required 3 s window. This procedure effectively solves the boundary discontinuity issue, at the cost of a slight but negligible reduction in the total micro-Doppler time analysis. Finally, the single micro-Doppler matrices are concatenated, and the merging procedure can be defined as:

$$M_{STFT} = M_1[t_1, t_1+L-\Delta] \cup \dots M_i[t_{i-1}+L-\Delta+\varepsilon, t_i+L-\Delta] \cup \dots \quad (7)$$

where M_{STFT} is the final micro-Doppler matrix, M_1 is the first STFT matrix, M_i is the i-th STFT matrix. The terms t_1 and t_i represent the starting time of the first and the i-th STFT interval, respectively. L denotes the duration of each segment on which the STFT is computed, and Δ is the time margin to ensure a proper overlap between consecutive matrices, which depends on the STFT parameters and segment overlap. The term ε prevents the last column of one matrix from being reused as the first column of the next matrix, and its value is derived from the STFT parameters. In this work L, Δ and ε are equal to 3, 0.1, and 0.01 s, respectively.

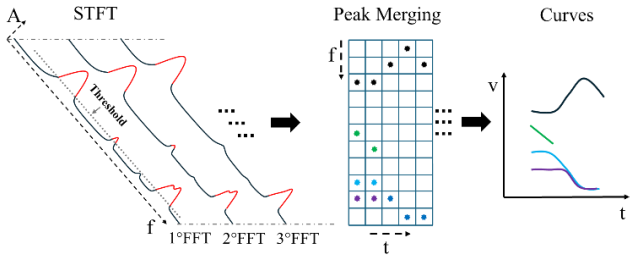

Fig. 3. Example of the curve extraction process

The resulting micro-Doppler matrices are merged by keeping the columns corresponding to [0 – 2.9] s from the first matrix, [2.91 – 5.7] s from the second matrix, [5.71-8.5] s from the third, and [8.51-11.3] s from the fourth.

B. Curve Extraction Algorithm

As shown in Fig. 3, the first step of the extraction involves identifying the peaks of the micro-Doppler curves in each column of the matrix. It is worth noting that the intensity of the micro-Doppler signature of a target can be associated with a bell curve on the frequency side. Consequently, each point of the column is first compared with an optimally chosen threshold, determined using established methods [43]. Consequently, the peaks are given by:

$$P(t_i, f_j) = \begin{cases} M(t_i, f_j) \text{ if } M(t_i, f_j) > Threshold \\ 0 \text{ otherwise} \end{cases} \quad (8)$$

where $P(t_i, f_j)$ is the peak value, $M(t_i, f_j)$ denotes the signal intensity at the i-th time t_i and the j-th frequency f_j. Afterward, the algorithm detects the maximum of every bell curve in the column. Therefore, the result is a matrix that contains the row number of the detected points for each curve present in the micro-Doppler signature.

The second step aims to form the curve vectors. Firstly, each point detected in a column is compared with the elements in the immediately adjacent right column. Points are grouped into the same curve vector if they satisfy a continuity criterion, specifically, if the difference in their row indices lies within a predefined interval, which can be tailored according to the specific application requirements. If the detected point is compatible with multiple elements of the previous column, the merger stops, and a new vector is initialized to avoid a potential incorrect point association. For example, when two contributions intersect in the micro-Doppler signature, the cross point is common to each vector curve. This creates ambiguity in how the algorithm will merge the successive points of the two contributions. Therefore, the fragmented curves are merged using a linear prediction model that estimates the next point in the curve. If a point from another curve is found to be closer to the predicted position, it is linked to the current curve vector. When no point is found in the next column, the algorithm searches up to three subsequent right columns. If no valid continuation is identified, the curve is considered completed. The nearby point in the same column may initially form two distinct curves. However, as the algorithm proceeds, they eventually cover the same points. The third step combines similar curves using a weighted average based on the intensity of their points for each column, as follows:

This work is licensed under a Creative Commons Attribution 4.0 License. For more information, see https://creativecommons.org/licenses/by/4.0/

This article has been accepted for publication in IEEE Sensors Journal. This is the author's version which has not been fully edited and
content may change prior to final publication. Citation information: DOI 10.1109/JSEN.2026.3692954

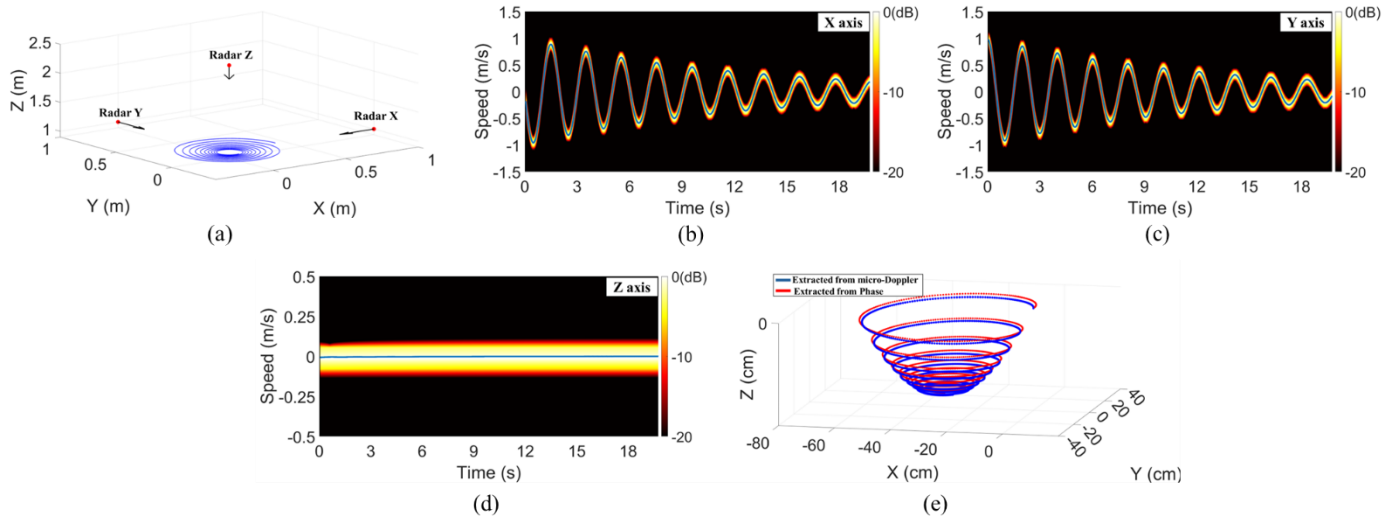

Fig. 4. (a) Simulated scenario. (b) Simulated micro-Doppler signatures and extracted velocity curves (blue line) for radar X, (c) radar Y, and (d) radar Z. (e) Three-dimensional displacement of the simulated scenario (blue curve, from micro-Doppler; red curve, from phase).

$$C_{merged}(t)=\sum_{i=1}^{n}\frac{I(C_i)\,C_i(t)}{I(C_i)} \tag{9}$$

where the parameter n is the number of curves, $C_i(t)$ is the i-th velocity curve, and $I(C_i)$ is the intensity of the i-th curve, which is based on the intensity of its points. Finally, the vector curves, mapped with the row indices, are converted into the velocity value given by considering the frequency vector obtained by applying (6) and employing (4). Therefore, the target displacement can be achieved by integrating the related velocity curve, as:

$$x(t)=\int_0^t v(t)dt \tag{10}$$

IV. Method Validation

Simulations and experimental scenarios were considered to evaluate the feasibility of three-dimensional displacement detection and extraction. The simulation and the first experiment serve as proofs of concept, aiming to assess whether radar sensors can effectively detect the target velocity. The second measurement focuses on a more realistic movement to extract the 3D trajectory of a human subject's center of mass.

A. Simulated Scenario

A point target was modeled to perform a damped conical pendulum motion, i.e., a damped circular motion along the X-Y plane, and a small height variation along the Z axis, due to air resistance. The presence of three 24 GHz Doppler radars was simulated along the orthogonal axes (X, Y, Z). Fig. 4(a) illustrates the simulated scenario and the target movement. The simulation starts with the target moving with an initial tangential speed of 1 m/s and a pendulum radius of approximately 30 cm. The total simulated time for the measurement is 20 s. An exponential decay function is applied to the velocity to simulate the damping effect caused by air resistance, resulting in a gradual decrease in both speed and pendulum radius over time, causing a displacement of a few centimeters along the Z axis. The baseband echo signals received by each Doppler radar sensor are analytically generated by computing the in-phase and quadrature components, which are obtained by converting the simulated trajectory of the target into proportional phase values. Thus, the two signals are combined to obtain the down-converted signal $S_b(t)$. Thus, the two signals are combined to obtain the down-converted signal $S_b(t)$. Applying the method described in Section III, the micro-Doppler signatures are obtained for each radar and shown in Fig. 4(b), (c), and (d). Although a motion is present along the Z-axis, this is performed for a relatively long time, i.e., 20 s. This corresponds to a non-zero but very low speed that cannot be detected due to the limitations illustrated in the next section. Fig. 4(e) shows the three-dimensional motion reconstructed from the micro-Doppler method (blue curve). The red curve represents the displacement from the phase-based (arctangent) method. The two curves are very similar, with minor differences due to the different processing techniques used. This is expected because, in the case of a single-point target, the classic phase-based method works well, and the related displacement fits very well the curve extracted from the micro-Doppler signature. Even though the presence of a single curve eases the algorithm burden, this is not the case in the real scenario shown in the next section, where the right curve is extracted also for a more complicated environment.

B. First Experimental Setup: Aluminum Sphere

The first experimental measurement reproduced the simulated scenario and used a stereophotogrammetric system as ground truth, i.e., a nine-camera stereophotogrammetric system (Vero 2.0, Vicon, Oxford Metrics, UK; sampling rate of 200 Hz). This single controlled measurement serves as a technical validation to verify the point-by-point correspondence between the radars and the high-precision reference system. The target was a 7 cm diameter aluminum sphere to ensure high electromagnetic and optical reflectivity. It was suspended by a 1.5 m long thread and anchored to an ad-hoc 2.5 m wooden structure, which also supports the Z-axis radar. The sensors along the X and Y axes were positioned at approximately 1.5 m from the target and elevated 1 m from the ground using tripods.

This work is licensed under a Creative Commons Attribution 4.0 License. For more information, see https://creativecommons.org/licenses/by/4.0/

This article has been accepted for publication in IEEE Sensors Journal. This is the author's version which has not been fully edited and
content may change prior to final publication. Citation information: DOI 10.1109/JSEN.2026.3692954

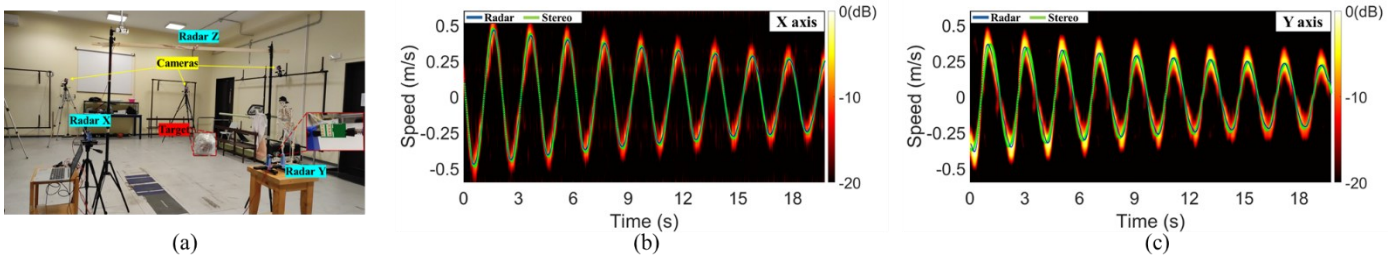

Fig. 5. (a). Picture of the first experimental measurement. (a) Measured micro-Doppler signature, velocity curves extracted from radar data (blue) and stereophotogrammetric reference (green) for radar X, (b) radar Y.

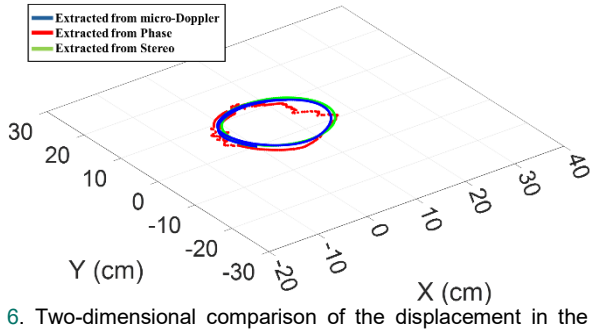

Fig. 6. Two-dimensional comparison of the displacement in the first experimental scenario: radar-estimated displacement (blue curve, from micro-Doppler), (red curve, from phase), and stereophotogrammetric reference (green curve).

Three Doppler radars, each based on the BGT24LTR11 transceivers by Infineon Technologies, were employed. They operate in the 24.0 – 24.25 GHz ISM band and have microstrip patch array antennas integrated with a 29x80° beamwidth and 10 dB gain. The Effective Isotropic Radiated Power (EIRP) for each radar is +14 dBm. To effectively cover the setup volume, the X and Y sensors were oriented to have their wider beam aligned with the motion plane. A DE10-Lite development board, based on the Intel MAX 10 10M50DAF484C7G Field Programmable Gate Arrays (FPGA), was used for signal management and synchronization with the stereophotogrammetric system. The FPGA performs the data acquisition of in-phase and quadrature signals for each radar at a sampling rate of 2.5 kHz, enabling the detection of velocity up to approximately 7 m/s. The acquired data are stored in onboard SDRAM and subsequently transmitted to a PC via a serial communication module. In addition, a Digital-To-Analog converter has been implemented in the FPGA to generate three distinct tuning voltages and set the radar operating frequencies to 24.060 GHz, 24.156 GHz, and 24.248 GHz, thus effectively avoiding mutual interferences. The physical connection is established using 3-meter-long cables, which transmit IF data, the analog tuning voltage, and the power supply.

Fig. 5(a) shows the experimental setup, including the target, the three radar sensors along the X, Y, and Z axes, and cameras. It is worth noting that the onboard 6Ch-ADC of the FPGA has a sampling time of 1 µs, resulting in a maximum time difference of 6 µs between the first and last sampled channels. Considering a maximum expected target speed of 1.5 m/s, the corresponding target displacement after 6 µs is approximately 9 µm. Therefore, this displacement is negligible, and the three radars can be considered synchronized for this study. Fig. 5(b) and (c) show the measured micro-Doppler signatures compared with the reference velocity profiles along the orthogonal axes.

TABLE I
CALCULATED DISPLACEMENT RMSE, VARIANCE VALUE, AND MAXIMUM ERROR FOR SPHERE TARGET

Target	Radar	RMSE (cm)	σ^2 (cm^2)	e_{max} (cm)
Spere	X	0.45	0.09	0.84
	Y	0.75	0.16	1.35

Moreover, the radar curves are also extracted to determine the similarity with the stereophotogrammetric system. To this aim, the root mean square error (RMSE) is calculated. From the results, the radar velocity curves on the X and Y axes closely match the reference measurements, with root mean square error (RMSE) values of 0.017 m/s and 0.036 m/s, respectively. The velocity along the Z-axis cannot be detected in this configuration. Indeed, according to (4), the Doppler shift is zero when the angle ψ between the target velocity vector and the radar Z LOS is exactly 90°. In this case, the low downward velocity of the target due to air friction produces a signal with a very low Doppler frequency. The passband of the amplification stage after the IQ mixer ranges from 23 Hz to 1.8 kHz.

Therefore, due to the low velocity, the received signal is not sufficiently amplified to be adequately detected. This is a limitation of many commercial Doppler radars equipped with ac-coupled receivers. Consequently, for very low speed, accurate displacement can only be obtained along the X and Y axes, where the measured curve and the reference are closely matched, as shown in Fig. 6. The results show that the radar sensor system accurately tracks the target velocity; meanwhile, the proposed method allows an accurate displacement evaluation, demonstrating the feasibility of the proposed approach, especially under favorable angular conditions. On the other hand, Fig. 6 shows that in the case of real multi-point targets, the classic phase-based method fails to detect the correct displacement, whereas the curves extracted from the micro-Doppler signature fit very well with the data measured by the stereophotogrammetric system. The RMSE, the variance (σ^2), and the maximum error (e_{max}) for the displacement are summarized in Table I.

C. Second Experimental Setup: Walking Human Subject

The second experiment involved a human participant (female, age: 44 years, height: 1.71 m, mass: 58 kg) walking on a treadmill at a constant speed of 4 km/h. The participant was enrolled only after signing written informed consent consistent with the Declaration of Helsinki. The study protocol was approved by the University of Bergamo Ethics Committee (approval code 2024_07_06). This measurement was conceived as a proof-of-concept to demonstrate the feasibility of the

This work is licensed under a Creative Commons Attribution 4.0 License. For more information, see https://creativecommons.org/licenses/by/4.0/

This article has been accepted for publication in IEEE Sensors Journal. This is the author's version which has not been fully edited and
content may change prior to final publication. Citation information: DOI 10.1109/JSEN.2026.3692954

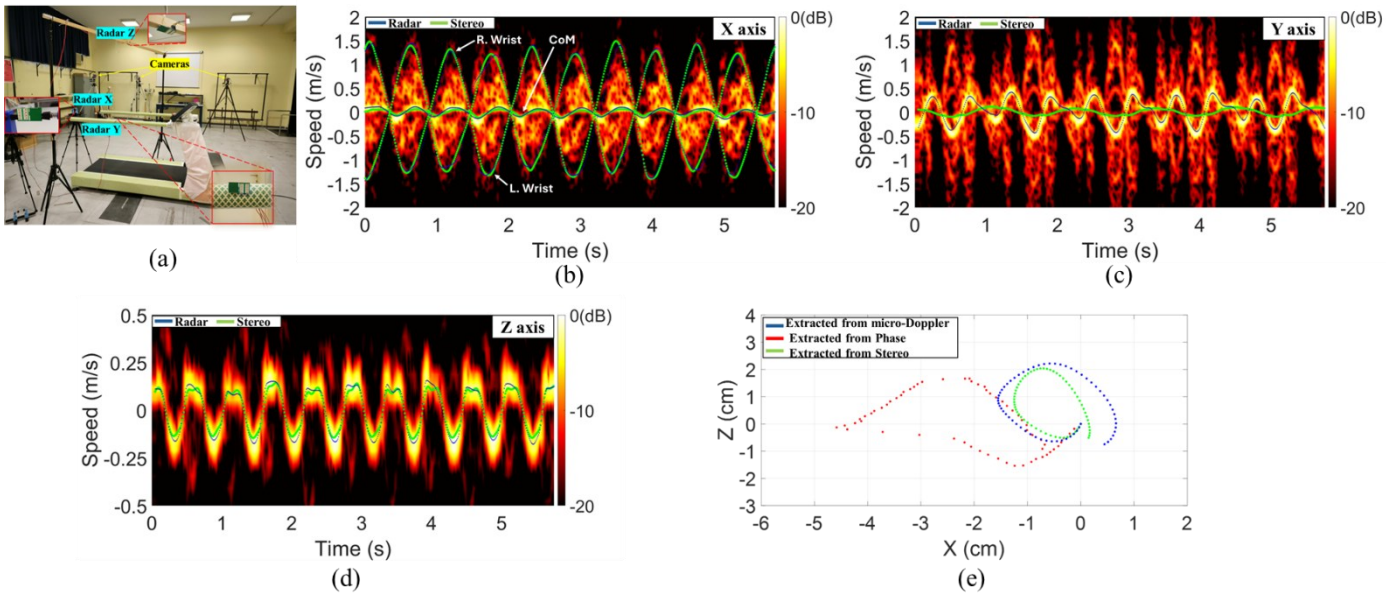

Fig. 7. (a) Picture of the second experimental measurement. (b). Comparison between velocity curve extracted from radar data (blue), and stereophotogrammetric reference (green) for radar X, (c) radar Y, and (d) radar Z micro-Doppler signatures. (e) 2D displacement, during normal walking at 4 km/h (red curve, displacement from phase).

proposed methodology. To consider the treadmill geometry and the need to observe motion along the anteroposterior, mediolateral, and craniocaudal directions, the X- and Y-axis radars were repositioned. The radar on the X axis was located behind the treadmill, approximately 1.5 m away from its center, thus minimizing the possible contribution of the treadmill's front cover. The radar sensor along the Y axis was placed on the side handrail, 50 cm from the center of the treadmill.

It is worth noting that for this type of antenna, the far field condition is satisfied for distances beyond 10 cm, given that the longest dimension of the antenna is 2.5 cm. Fig. 7(a) illustrates the final configuration of the radar-treadmill setup. The stereophotogrammetric system recorded the three-dimensional trajectories of 18 passive reflective markers that were attached to the participant to define an 11-segment model according to [44],[45].

The body center of mass trajectory was subsequently obtained using Dempster's segmental inertial parameters, as the weighted mean of the center-of-mass trajectories of the individual segments [46]. Finally, the body center of mass velocity was obtained via differentiation of its trajectory. The radar ability to detect this parameter highlights its potential as a viable, non-invasive alternative for human gait analysis.

Two sessions of measurement were conducted: in the former, the participant walked normally; in the latter, the participant was instructed to keep the arms as still as possible to reduce the components caused by arm swinging in the radar micro-Doppler measurement. Fig. 7 (b), (c), and (d), and Fig. 8 show the micro-Doppler signatures obtained during the two walking trials, compared to the reference provided by the stereophotogrammetric system. It is worth noting that micro-Doppler measurements exhibit a periodic pattern due to the treadmill setup. Indeed, the treadmill's presence forces the subject to move on the same point, thus making any movements periodic with a null average speed. Along the X axis, the high-intensity components centered around 0 m/s indicate the velocity of the center of mass. The comparison between the two trials also shows strips extending up to ± 1.5 m/s, roughly corresponding to the motion of the arms during the gait cycle.

As demonstrated in Fig. 8(b), the proposed method is capable of extracting multiple, distinct speed curves from a single micro-Doppler measurement, which provides a clearer representation of the individual body part motions. Along the Y axis, the components caused by swinging arms complicate the analysis and reduce the ability to detect the lateral component of the center of mass velocity during natural walking. Moreover, the minimal radial displacement along the Y axis is captured by radar due to the large radar cross-section of the human body.

Conversely, the Z-axis signature is primarily generated by the vertical movement of the subject's head, effectively capturing the vertical velocity of the center of mass since the vertical oscillation of the head is closely correlated with the vertical displacement of the body while walking. As expected, Fig. 8(e) shows that the displacement extracted through the phase-based method leads to an incorrect estimation. Finally, Fig. 9 shows the three-dimensional trajectory of the center of mass, estimated by the radar system and the reference stereophotogrammetric system during the trial with arm swing suppression. Moreover, Fig. 9(a), once more, shows that the displacement extracted by the phase-based method leads to incorrect displacement, making it unsuitable for 3D displacement measurements. It is important to note that in Fig. 7(e) and Fig. 8, only a time interval of the full measurement is displayed to enhance visualization of the displacement trend and better emphasize the comparison. Specifically, the time interval shown is 3.18 - 3.8 s in Fig. 7(e) and 0.5 - 1.3 s in Fig.8. As reported in Table II, the obtained RMSE, maximum error, and variance can be considered quite satisfactory; indeed, it is worth noting that the body center of mass measurements are indirect measurements referred to a point inside the participant's body whose range of movement along the three considered axes is in the order of centimeters, depending on the direction [47]. Apart from the Y-axis during typical walking with free arms, an error in the order of

This work is licensed under a Creative Commons Attribution 4.0 License. For more information, see https://creativecommons.org/licenses/by/4.0/

This article has been accepted for publication in IEEE Sensors Journal. This is the author's version which has not been fully edited and
content may change prior to final publication. Citation information: DOI 10.1109/JSEN.2026.3692954

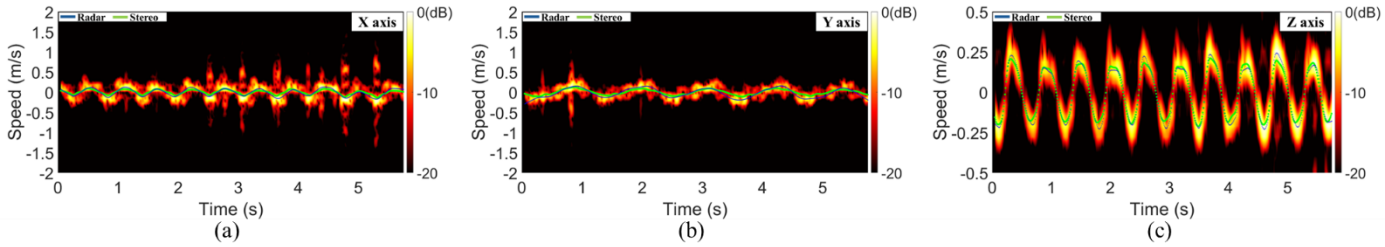

Fig. 8. Comparison between micro-Doppler signature, radar-extracted velocity (blue), and stereophotogrammetric reference (green) for (a) radar X, (b) radar Y, and (c) radar Z during 4 km/h walking without arm swing.

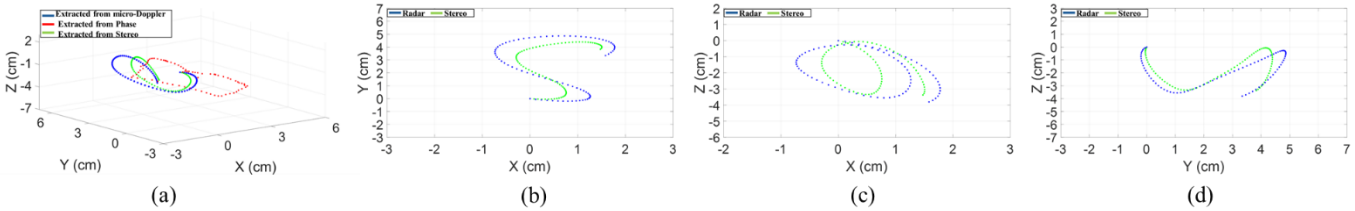

Fig. 9. (a) 3D center of mass displacement, (b) XY, (c) XZ, and (d) YZ planes extracted by radar (blue curve, from micro-Doppler), (red curve, from phase), and stereophotogrammetric reference (green curve).

TABLE II
CALCULATED DISPLACEMENT RMSE, VARIANCE VALUE, AND MAXIMUM ERROR FOR HUMAN TARGET

Walk	Radar	RMSE (cm)	σ^2 (cm^2)	e_{max} (cm)
With Arms	X	0.29	0.07	0.54
	Y	1.91	3.11	3.65
	Z	0.13	0.02	0.23
No Arms	X	0.34	0.09	0.59
	Y	0.34	0.33	0.65
	Z	0.16	0.14	0.34

millimeters has been obtained using contactless tracking of external movements of a subject walking on a treadmill.

These findings demonstrate that micro-Doppler-based displacement estimation offers a robust alternative for motion tracking, especially in scenarios where phase-based techniques are limited by target stationarity or complex motions. Furthermore, the results underline the strong potential of radar-based systems in human gait analysis and body center of mass estimation.

V. CONCLUSION

This study presents a proof-of-concept for 3D displacement estimation via Doppler radars by isolating velocity components from micro-Doppler signatures. Validated through simulations and experiments on a spherical target, the method showed strong agreement with stereophotogrammetric ground truth.

Additionally, its applicability to real-world scenarios was preliminarily confirmed in a human walking trial involving one participant to track the motion of the body's center of mass. The limitations of the method include dependence on sufficiently strong micro-Doppler components, reduced sensitivity to very low-velocity and line-of-sight-orthogonal motions.

Future work will be aimed at improving the lateral movement detection with the swinging arms and at validating the algorithm performance by extending the experimental dataset with a higher number of participants with different heights, step frequencies, and gait conditions (e.g., different walking speeds and/or overground walking).

REFERENCES

[1] F. Michler, B. Scheiner, T. Reissland, R. Weigel, and A. Koelpin, "Micrometer Sensing With Microwaves: Precise Radar Systems for Innovative Measurement Applications," *IEEE J. Microw.*, vol. 1, no. 1, pp. 202–217, Jan. 2021, doi: 10.1109/JMW.2020.3034988.

[2] A. C. Amies, C. G. Pretty, G. W. Rodgers, and J. G. Chase, "Experimental Validation of a Radar-Based Structural Health Monitoring System," *IEEE/ASME Trans. Mechatron.*, vol. 24, no. 5, pp. 2064–2072, Oct. 2019, doi: 10.1109/TMECH.2019.2934091.

[3] S. Dong *et al.*, "A Review on Recent Advancements of Biomedical Radar for Clinical Applications," *IEEE Open J. Eng. Med. Biol.*, vol. 5, pp. 707–724, 2024, doi: 10.1109/OJEMB.2024.3401105.

[4] A. A. Pramudita, D.-B. Lin, A. A. Dhiyani, H. H. Ryanu, T. Adiprabowo, and E. A. Yudha, "FMCW Radar for Noncontact Bridge Structure Displacement Estimation," *IEEE Trans. Instrum. Meas.*, vol. 72, pp. 1–14, 2023, doi: 10.1109/TIM.2023.3292960.

[5] E. Cardillo, L. Ferro, and C. Li, "Microwave and Millimeter-Wave Radar Circuits for the Next Generation Contact-Less In-Cabin Detection," in 2022 *Asia-Pacific Microwave Conference (APMC)*, Yokohama, Japan, 2022, pp. 231-233, doi: 10.23919/APMC55665.2022.9999764..

[6] M. T. Buyukakkaslar, M. A. Erturk, and M. A. Aydin, "A Review on Radar-Based Human Detection Techniques," *Sensors*, vol. 24, no. 17, p. 5709, Sep. 2024, doi: 10.3390/s24175709.

[7] W. Song, Y. Yang, M. Fu, F. Qiu, and M. Wang, "Real-Time Obstacles Detection and Status Classification for Collision Warning in a Vehicle Active Safety System," *IEEE Trans. Intell. Transport. Syst.*, vol. 19, no. 3, pp. 758–773, Mar. 2018, doi: 10.1109/TITS.2017.2700628.

[8] E. Cardillo, L. Ferro, G. Sapienza and C. Li, "Reliable Eye-Blinking Detection With Millimeter-Wave Radar Glasses," in *IEEE Transactions on Microwave Theory and Techniques*, vol. 72, no. 1, pp. 771-779, Jan. 2024, doi: 10.1109/TMTT.2023.3329707.

[9] E. Cardillo, G. Sapienza, L. Ferro, C. Li and A. Caddemi, "Radar Assistive System for People with Neurodegenerative Disorders Through Head Motion and Eyes Blinking Detection," 2023 IEEE/MTT-S International Microwave Symposium - IMS 2023, San Diego, CA, USA, 2023, pp. 979-982, doi: 10.1109/IMS37964.2023.10187979.

[10] E. Cardillo and C. Li, *Portable Microwave and mmWave Radars for Contactless Healthcare*, Denmark, River Publishers, Dec. 2024.

[11] X. Gao, J. Xu, A. Rahman, V. Lubecke, and O. Boric-Lubecke, "Arc shifting method for small displacement measurement with quadrature CW doppler radar," in *2017 IEEE MTT-S International Microwave Symposium (IMS)*, Honolulu, HI, USA: IEEE, Jun. 2017, pp. 1003–1006. doi: 10.1109/MWSYM.2017.8058760.

[12] T. Kinoshita and H. Yamada, "Vibration Disturbance Cancellation Method for Estimation of Target Displacement by CW Doppler Radar,"

This work is licensed under a Creative Commons Attribution 4.0 License. For more information, see https://creativecommons.org/licenses/by/4.0/

This article has been accepted for publication in IEEE Sensors Journal. This is the author's version which has not been fully edited and
content may change prior to final publication. Citation information: DOI 10.1109/JSEN.2026.3692954

in *2020 IEEE Radar Conference (RadarConf20)*, Florence, Italy: IEEE, Sep. 2020, pp. 1–5. doi: 10.1109/RadarConf2043947.2020.9266469.

[13] H. Wang, H. Afzal, and O. Momeni, "A Highly Accurate and Sensitive mmWave Displacement-Sensing Doppler Radar With a Quadrature-Less Edge-Driven Phase Demodulator," *IEEE J. Solid-State Circuits*, vol. 58, no. 9, pp. 2451–2465, Sep. 2023, doi: 10.1109/JSSC.2023.3266704.

[14] Q. Lv *et al.*, "Accurate Sensing of Arbitrary Displacement Motions Based on Polar Chord Accumulation With Interferometric Radar," *IEEE Trans. Microwave Theory Techn.*, vol. 72, no. 12, pp. 6983–6995, Dec. 2024, doi: 10.1109/TMTT.2024.3412672.

[15] J.-H. Parkl, J.-Y. Sim, and J.-R. Yang, "Multi-Phase CW Doppler Radar for Measuring Small Periodic Displacement," in *2020 17th European Radar Conference (EuRAD)*, Utrecht, Netherlands: IEEE, Jan. 2021, pp. 86–89. doi: 10.1109/EuRAD48048.2021.00033.

[16] Jia Xu, Xiaomeng Gao, B. E. Padasdao, and O. Boric-Lubecke, "Estimation of physiological sub-millimeter displacement with CW Doppler radar," in *2015 37th Annual International Conference of the IEEE Engineering in Medicine and Biology Society (EMBC)*, Milan: IEEE, Aug. 2015, pp. 7602–7605. doi: 10.1109/EMBC.2015.7320152.

[17] L. Ferro, G. Scandurra, C. Ciofi and E. Cardillo, "An Insight into the Displacement Evaluation during Real-Time Radar Measurements," in *IEEE Sensors Journal*, doi: 10.1109/JSEN.2025.3594433.

[18] L. Ferro, C. Li, G. Scandurra, C. Ciofi, and E. Cardillo, "Beneficial Effects of Self-Motion for the Continuous Phase Analysis of Ac-Coupled Doppler Radars," *Electronics*, vol. 13, no. 4, p. 772, Feb. 2024, doi: 10.3390/electronics13040772.

[19] L. Ferro, G. Scandurra, C. Li, and E. Cardillo, "Robust Doppler Displacement Measurement Resolving the Uncertainty During Target Stationary Moment," in *2024 IEEE Topical Conference on Wireless Sensors and Sensor Networks (WiSNeT)*, San Antonio, TX, USA: IEEE, Jan. 2024, pp. 57–60. doi: 10.1109/WiSNeT59910.2024.10438649.

[20] D. Xu, W. Yu, Y. Wang, and M. Chen, "Vital Signs Detection in the Presence of Nonperiodic Body Movements," *IEEE Trans. Instrum. Meas.*, vol. 73, pp. 1–16, 2024, doi: 10.1109/TIM.2024.3450071.

[21] G. Beltrão, T. Feuillen, M. R. B. Shankar, M. Alaee-Kerahroodi, and U. Schroeder, "Unlimited Sampling for Radar-based Vital Sign Monitoring," in *2022 56th Asilomar Conference on Signals, Systems, and Computers*, Pacific Grove, CA, USA: IEEE, Oct. 2022, pp. 1131–1136. doi: 10.1109/IEEECONF56349.2022.10051975.

[22] F. Zhu, K. Wang, and K. Wu, "Doppler Radar Techniques for Vital Signs Detection Featuring Noise Cancellation," in *2019 IEEE MTT-S International Microwave Biomedical Conference (IMBioC)*, Nanjing, China: IEEE, May 2019, pp. 1–4. doi: 10.1109/IMBIOC.2019.8777824.

[23] B. Falęcki, K. Abratkiewicz and P. Samczyński, "Measurement of Human Vital Signs Based on High-Resolution mmWave Micro-Doppler Radar Signatures," *2024 International Radar Symposium (IRS)*, Wroclaw, Poland, 2024, pp. 260-265.

[24] M. Nosrati and N. Tavassolian, "High-Accuracy Heart Rate Variability Monitoring Using Doppler Radar Based on Gaussian Pulse Train Modeling and FTPR Algorithm," *IEEE Trans. Microwave Theory Techn.*, vol. 66, no. 1, pp. 556–567, Jan. 2018, doi: 10.1109/TMTT.2017.2721407.

[25] F. Cai, A. Patharkar, T. Wu, F. Y. M. Lure, H. Chen, and V. C. Chen, "STRIDE: Systematic Radar Intelligence Analysis for ADRD Risk Evaluation With Gait Signature Simulation and Deep Learning," *IEEE Sensors J.*, vol. 23, no. 10, pp. 10998–11006, May 2023, doi: 10.1109/JSEN.2023.3263071.

[26] C. Ding, J. Weng, H. Zhao, Q. Zhou, H. Hong, and X. Zhu, "Omnidirectional Human Activity Recognition With Spatial–Temporal Trajectory-Based Compensation Using Monostatic MIMO Radar," *IEEE Trans. Microwave Theory Techn.*, pp. 1–13, 2025, doi: 10.1109/TMTT.2025.3530533.

[27] M. G. Benedetti *et al.*, "SIAMOC position paper on gait analysis in clinical practice: General requirements, methods and appropriateness. Results of an Italian consensus conference," *Gait & Posture*, vol. 58, pp. 252–260, Oct. 2017, doi: 10.1016/j.gaitpost.2017.08.003.

[28] R. Ranjan, D. Ahmedt-Aristizabal, M. Ali Armin and J. Kim, "Computer Vision for Clinical Gait Analysis: A Gait Abnormality Video Dataset," in *IEEE Access*, vol. 13, pp. 45321-45339, 2025, doi: 10.1109/ACCESS.2025.3545787.

[29] J. R. A. Castillo *et al*., "Mitigating Drift in Extraction of Joint Angle Measurements from Inertial Measurement Unit (IMU) Data," *TENCON 2024 - 2024 IEEE Region 10 Conference (TENCON)*, Singapore, Singapore, 2024, pp. 666-669, doi: 10.1109/TENCON61640.2024.10902826.

[30] S. Ashry, S. Das, M. Rafiei, J. Baumbach and L. Baumbach, "Transfer Learning of Human Activities Based on IMU Sensors: A Review," in *IEEE Sensors Journal*, vol. 25, no. 3, pp. 4115-4126, Feb 2025, doi: 10.1109/JSEN.2024.3510097.

[31] A.-K. Seifert, M. Grimmer, and A. M. Zoubir, "Doppler Radar for the Extraction of Biomechanical Parameters in Gait Analysis," May 11, 2020, *arXiv*: arXiv:2005.05280. doi: 10.48550/arXiv.2005.05280.

[32] K. Saho, K. Shioiri, S. Kudo, and M. Fujimoto, "Estimation of Gait Parameters From Trunk Movement Measured by Doppler Radar," *IEEE J. Electromagn. RF Microw. Med. Biol.*, vol. 6, no. 4, pp. 461–469, Dec. 2022, doi: 10.1109/JERM.2022.3198814.

[33] K. Saho, K. Sugano, M. Kita, K. Uemura, and M. Matsumoto, "Classification of Health Literacy and Cognitive Impairments Using Higher-Order Kinematic Parameters of the Sit-to-Stand Movement From a Monostatic Doppler Radar," *IEEE Sensors J.*, vol. 21, no. 8, pp. 10183–10192, Apr. 2021, doi: 10.1109/JSEN.2021.3060050.

[34] V. C. Chen, *The micro-Doppler effect in radar*, Second edition. in Artech House radar library series. Boston London: Artech House, 2019.

[35] P. Zhang, W. Xie, J. Ou, J. Zhang, K. Liu, and G. Wang, "Research on Human Micro-motion Feature Extraction Technology," *2019 IEEE 3rd Advanced Information Management, Communicates, Electronic and Automation Control Conference (IMCEC)*, Chongqing, China, 2019, pp. 762-767, doi: 10.1109/IMCEC46724.2019.8983848.

[36] A.-K. Seifert, M. G. Amin, and A. M. Zoubir, "Toward Unobtrusive In-home Gait Analysis Based on Radar Micro-Doppler Signatures," *IEEE Trans. Biomed. Eng.*, vol. 66, no. 9, pp. 2629–2640, Sept. 2019, doi: 10.1109/TBME.2019.2893528.

[37] A. G. Arguello and D. Berges, "Radar Classification for Traffic Intersection Surveillance based on Micro-Doppler Signatures," in *2018 15th European Radar Conference (EuRAD)*, Madrid: IEEE, Sept. 2018, pp. 186–189. doi: 10.23919/EuRAD.2018.8546545.

[38] B. Debnath, I. A. Ebu, S. Biswas, A. C. Gurbuz, and J. E. Ball, "FMCW Radar Range Profile and Micro-Doppler Signature Fusion for Improved Traffic Signaling Motion Classification," in *2024 IEEE Radar Conference (RadarConf24)*, Denver, CO, USA: IEEE, May 2024, pp. 1–6. doi: 10.1109/RadarConf2458775.2024.10548322.

[39] I. Garvanov, M. Garvanova, D. Borissova, M. Cvjetkovic, J. Nikic, and M. Tomov, "Analysis of Micro-Doppler Signatures for Drone Detection," in 2025 19th Conference on Electrical Machines, Drives and Power Systems (ELMA), Sofia, Bulgaria: IEEE, June 2025, pp. 1–5. doi: 10.1109/ELMA65795.2025.11083508.

[40] J. Hu, "Three-dimensional interferometric imaging and precession feature extraction of space targets in wideband radar," *J. Appl. Rem. Sens.*, vol. 12, no. 01, p. 1, Mar. 2018, doi: 10.1117/1.JRS.12.016029.

[41] J. Hu, Y. Luo, Q. Zhang, and Y. T. Soon, "Three-dimensional interferometric imaging and micromotion feature extraction of spinning space debris in low-resolution radar," *J. Appl. Rem. Sens.*, vol. 12, no. 04, p. 1, Oct. 2018, doi: 10.1117/1.JRS.12.046013.

[42] P. Brasiliano, F. L. Carcione, G. Pavei, E. Cardillo and E. Bergamini, "Radar-Based Deep Learning for Gait Smoothness Estimation: A Feasibility Study," *2025 IEEE Medical Measurements & Applications (MeMeA)*, Chania, Greece, 2025, pp. 1-6, doi: 10.1109/MeMeA65319.2025.11068038.

[43] Z. Liang, J. Gai, X. Chen, T. Ma, and Q. Liu, "A Method for Threshold Setting and False Alarm Probability Evaluation for Radar Detectors," *Signal Processing*, vol. 207, p. 108930, Jun. 2023, doi: 10.1016/j.sigpro.2023.108930.

[44] A. E. Minetti, L. P. Ardigò, and F. Saibene, "Mechanical determinants of gradient walking energetics in man.," *J. Physiol.*, vol. 472, pp. 725–735, Dec. 1993, doi: 10.1113/jphysiol.1993.sp019969.

[45] G. Pavei, F. Salis, A. Cereatti, and E. Bergamini, "Body center of mass trajectory and mechanical energy using inertial sensors: a feasible stride?," *Gait Posture*, vol. 80, pp. 199–205, Jul. 2020, doi: 10.1016/j.gaitpost.2020.04.012.

[46] W. T. Dempster, W. C. Gabel, and W. J. Felts, "The anthropometry of the manual work space for the seated subject," *Am. J. Phys. Anthropol.*, vol. 17, no. 4, pp. 289–317, Dec. 1959, doi: 10.1002/ajpa.1330170405.

[47] A. E. Minetti, C. Cisotti, and O. S. Mian, "The mathematical description of the body centre of mass 3D path in human and animal locomotion," *J. Biomech*., vol. 44, no. 8, pp. 1471–1477, 2011, doi: 10.1016/j.jbiomech.2011.03.014.

This work is licensed under a Creative Commons Attribution 4.0 License. For more information, see https://creativecommons.org/licenses/by/4.0/